

Ti-Based Surface Integrated Layer and Bulk Doping for Stable Voltage and Long Life of Li-Rich Layered Cathodes

Dong Luo, Jiaxiang Cui, Bingkai Zhang, Jianming Fan, Peizhi Liu, Xiaokai Ding, Huixian Xie, Zuhao Zhang, Junjie Guo, Feng Pan, and Zhan Lin*

High-energy-density lithium-rich layered oxides (LLOs) hold the greatest promise to address the range anxiety of electric vehicles. Their application, however, has been prevented by fast voltage decay and capacity fading for years, which mainly originate from irreversible transition-metal migration and undesirable cathode-electrolyte interfacial reactions. Herein, a Ti-based surface integrated layer and bulk doping, which greatly improve the voltage and capacity stability of LLOs is synchronously constructed. More importantly, STEM and Raman results demonstrate that continuous and uniform surface Ti-based integrated layer is a spinel-like rocksalt structure with Fd-3m space group, which is built through by several the replacement of Li ions in surface several atomic layers by Ti ions. After 500 cycles, Ti-150 sample delivers a capacity retention of 85%, and its voltage decay rate from the 30th to the 500th cycle is only ≈0.72 mV/cycle. Spectral results and DFT calculations suggest that bulk Ti-doping mitigates the migration of Mn and Ni ions in the bulk, while Ti-based integrated layer significantly suppresses surface structure evolution and interfacial reactions by impeding the generation of surface Li vacancies during Li extraction as well as preventing direct contact between electrolyte and active materials.

1. Introduction

The ubiquity of consumer electronics and rapid development of electric vehicles require next-generation lithium-ion batteries with higher energy density and longer life, both of which are mainly limited by cathode materials.^[1] Among the various cathodes investigated to date, Li-rich layered oxides (LLOs) have attracted widespread attention due to their extraordinarily high reversible capacity (>250 mAh g⁻¹).^[2] It was well documented that extraordinary capacity of LLOs is attributed to cumulative

contribution of both cationic and anionic reversible redox processes under high operating voltage (>4.6 V).^[3] Unfortunately, the practical application of LLOs is still hampered by severe voltage decay and capacity fading, mostly due to continuous transition metal (TM) migration and resultant gradual structural evolution from layered to spinel or rocksalt phase.^[4]

TM migration or structural evolution is well known to start from the surface of LLO cathodes during cycling.^[5] The generation of Li vacancies upon delithiation and serious cathode-electrolyte interfacial reactions at high operating voltage provide fundamental driving force for the migration of surface TM ions.^[6] Li vacancies lead to severe distortion of TMO₆ octahedron and decrease the energy barrier of TM migration, both of which promote TM ions migration into the Li-layer.^[7] Interfacial reactions typically give rise to surface TM dissolution, corrosion and oxygen vacancies, promoting

the surface TM migration.^[8] In addition, interfacial reactions also induce the reduction of Mn⁴⁺ to Mn³⁺ ions upon cycling, which are known to be vulnerable to migration.^[9] The synergistic contribution of these two inducements makes the surface TM migration or structural evolution easy to be observed. Although most of TM migration or structural evolution is usually observed on the surface, it is demonstrated to propagate gradually into the bulk.^[10] These suggest that surface protection and defense against structural evolution towards the bulk are still very essential.

Dr. D. Luo, J. Cui, Dr. B. Zhang, X. Ding, H. Xie, Z. Zhang, Prof. Z. Lin Guangzhou Key Laboratory of Clean Transportation Energy Chemistry School of Chemical Engineering and Light Industry Guangdong University of Technology Guangzhou 510006, China E-mail: zhanlin@gdut.edu.cn
Dr. J. Fan Fujian Provincial Key Laboratory of Clean Energy Materials College of Chemistry and Materials Longyan University Longyan 364012, China

Dr. P. Liu, Prof. J. Guo
Key Laboratory of Interface Science and Engineering
in Advanced Materials
Ministry of Education
Taiyuan University of Technology
Taiyuan 030024, China
Prof. F. Pan
School of Advanced Materials
Shenzhen Graduate School
Peking University
Shenzhen, China

The ORCID identification number(s) for the author(s) of this article can be found under https://doi.org/10.1002/adfm.202009310.

DOI: 10.1002/adfm.202009310

www.afm-journal.de

1616292. 2021, 14, Downloaded from https://advanced.onlinelibtrary.viely.com/doi/10.1002/adf.202009310 by University Town Of Shenzhen, Wiley Online Library on [24/11/2025]. See the Terms and Conditions (https://onlinelibrary.wiley.com/terms-and-conditions) on Wiley Online Library or rules of use; OA articles are governed by the applicable Creative Commons License

Due to strong Ti-O bonds and stable valence, [7c] Ti4+-based modifications (i.e., bulk doping or surface coating in Table S1. Supporting Information) have been used to improve the electrochemical performance of layered cathodes.[11] Although Ti-based bulk doping has the effect of stabilizing structure and mitigating surface structural evolution towards the bulk, it does not insulate active material from contact with the electrolyte and hardly suppresses interfacial reactions. Ti-based coating effectively restrains direct contact of cathode and electrolyte, but it cannot prevent structural evolution from permeating into the bulk. What's more, Ti ions are very hard to effectively occupy surface Li sites of lithium layer by the above two traditional Ti-based modified strategies. Both of them fail to suppress the generation of surface Li vacancies during Li extraction, which may be achieved through the replacement of Li ions on surface several atomic layers by electrochemical inert cationic ions.^[12] Therefore, it is very critical to build up combinative protection of the surface and the bulk to effectively mitigate the voltage decay and capacity fading of LLO cathodes. However, the construction of the above-mentioned dual protection system by one-step treated strategy still remains a significant challenge, especially suppressing the generation of surface Li vacancies.

In this work, we synchronously construct bulk Ti-doping and surface Ti-based integrated layer by a molten-salt-assisted solvothermal-treatment method. Aberration-corrected high-angle annular-dark-field scanning transmission electron microscopy (HAADF-STEM) and Raman spectra prove that continuous and uniform Ti-based surface integrated layer is a spinel-like rocksalt structure with Fd-3m space group. It is achieved through the replacement of Li ions by Ti ions on surface in several atomic. Thus, this Ti-based surface integrated layer effectively inhibits interfacial reactions and the generation of surface Li vacancies, resulting in a slow TM migration or structural evolution. Electrochemical measurement demonstrates that the combination of Ti-based surface integrated layer and bulk Tidoping greatly improves the voltage and capacity stability of LLOs. After 500 cycles, Ti-150 sample delivers a capacity retention of 85%, and its voltage decay rate from 30th to 500th cycle is only ≈0.72 mV/cycle. In addition, the comparative data of this work and representative Ti-based coating or doping references also suggest the dual protective systems effectively enhance the voltage and capacity stability of LLOs, as shown in Table S1, Supporting Information. This work provides a new strategy to enhance both the voltage and capacity stability by the construction of surface Ti-based integrated layer and its combination with bulk doping, which is conducive to the practical application of LLO cathodes in the near future.

2. Results and Discussion

The Ti-treated samples were obtained by the combination of solvothermal reaction based on a cladding-regrowth process and sintering procedure, as shown in **Figure 1a**. Under the solvothermal condition, $C_{16}H_{36}O_4Ti$ is slowly hydrolyzed into Ti species which uniformly coat on the surface of the precursor. After sintering with Li_2CO_3 , Ti^{4+} ions are successfully doped into the surface lattices of LLO materials. The structure and morphology of as-prepared samples were systematically

examined by X-ray Powder Diffraction (XRD), scanning electron microscope (SEM) and STEM. XRD patterns of pristine (PM) and Ti-treated samples are shown in Figure S1, Supporting Information. All samples exhibit similar XRD patterns. The relatively strong diffraction peaks are well indexed to the hexagonal α -NaFeO₂ structure, [13] a typical layered-type structure with the space group R3-m, while the few weak peaks between 20° and 25° are attributed to the monoclinic Li₂MnO₃ phase with the space group C/2m. [14] Moreover, the very small peak at \approx 30° of XRD patterns for 0.1% and 0.3% Ti sample (Figure S1a, Supporting Information) can be indexed to Li₂CO₃. The pair reflections (006)/(012) and (018)/(110) for all samples are well separated, indicating that all samples have high crystal-linity, good hexagonal ordering, and layered characteristics. [15]

Cycling performance of all samples are compared in Figure S2, Supporting Information. The obvious difference in capacity of Ti-150 and Ti-200 samples is mainly because high treated temperature of solvothermal reaction results in large primary particles, as presented in Figure S3, Supporting Information. Considering that the samples treated with 0.5 mol% Ti under 100 °C (Ti-100) and 150 °C (Ti-150) delivers better comprehensive electrochemical performance than others, we will focus on the comparative study of Ti-100, Ti-150, and PM samples. Lattice parameters of PM, Ti-100, and Ti-150 samples were further examined through structural refinement with the program GSAS, as presented in Figure 1b-d. The axis ratio c/a of all the three samples is close to 4.98 (Table S2, Supporting Information), which indicates that the introduction of Ti⁴⁺ does not obviously change the lattice parameters of as-prepared samples. This is because the radius of Ti⁴⁺ lies between that of Mn⁴⁺, Ni²⁺, and Li⁺, and Ti⁴⁺ occupies synchronously the sites of these three cations. SEM images of the three samples are shown Figure 1e-g. PM and Ti-100 samples present assembled microspheres with a diameter distribution in the range 5-10 µm, while most of the microspheres for Ti-150 sample suffer from severe destruction. Too much high treated-temperature leads to a fast hydrolysis of C₁₆H₃₆O₄Ti which is not conducive to maintaining the morphology of assembled microspheres.

To further understand the structure of Ti-treated samples, aberration-corrected HAADF-STEM was employed to visually observe atomic arrangement (**Figure 2**). As displayed in Figure 2b, the *d*-spacings of three singed diffraction spots are 4.72, 2.36 and 2.41Å, respectively. These values are in accord with (003), (006) and (101) facets of R-3m layer structure. As shown in Figure 2c–e, an interlayer spacing of 0.47 or 0.48 nm is observed from different regions, corresponding to the (003) plane of LiMO₂ or the (001) plane of Li₂MnO₃. The selected areas in Figure 2c,d demonstrate that Ti atoms are evenly embedded in the surface of particles and form a stable and continuous Ti-based integrated layer.

In addition, the regions g, h, and i of Figure 2f,h are selected to probe the evolution of surface structure after modification. Figure 2g-i clearly demonstrates that the sample is a two-phase structure. Its bulk phase is the layered phase and its surface is composed of a spinel-like rocksalt structure Fd-3m phase with a thickness about 2 nm (Figure 2c,d). On the surface several atom layers, Li atoms are replaced by Ti atoms, suggesting that Ti-based integrated layer is established. Note that we tried to provide some overview STEM images as strong evidence for

16163028, 2021, 14, Downloaded from https://advanced.onlinelibrary.wiley.com/doi/10.1002/adfm.202009310 by University Town Of Shenzhen, Wiley Online Library on [2411/2025]. See the Terms

onditions) on Wiley Online Library for rules of use; OA articles are governed by the applicable Creative Commons

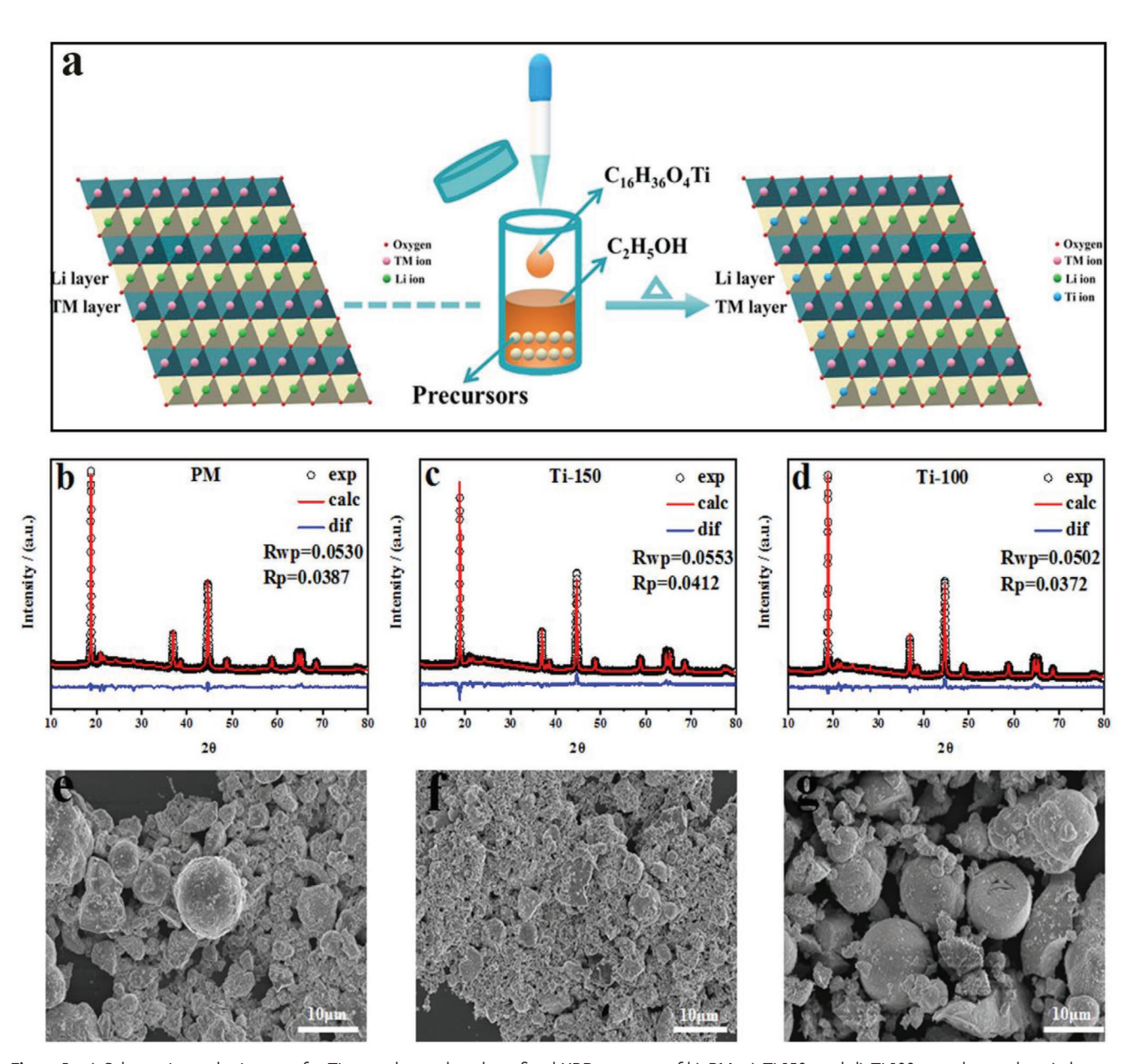


Figure 1. a) Schematic synthetic route for Ti-treated samples; the refined XRD patterns of b) PM, c) Ti-150, and d) Ti-100 samples, and e-g) the corresponding SEM images.

surface fully replaced regions. However, it is very difficult to observe atom distribution in overview STEM images due to limited magnification. Therefore, STEM images with medium magnification (Figure S4, Supporting Information) were employed, in which atomic distribution between the surface and the bulk is observed faintly. For a clear view, the randomly selected HADDF-STEM images (Figure 2c-i) were investigated. Surface Ti-based integrated layer in all these HADDF-STEM images is continuous and uniform. Based on the above evidences, we believe that a Ti-based integrated layer has been achieved in our Ti-treated samples. This continuous and uniform Ti-based integrated layer serves as a stable wall which will protect LLO cathodes from the corrosion of electrolyte and suppress the surface TM dissolution.

In the bulk, the cross-section SEM-EDX maps (Figure S5, Supporting Information) demonstrate that Ti atoms occupy part TM lattices, which act as the second defensive line to impede bulk TM migration. Notably, there are some work about Li-sites partially doped by electrochemical inert cationic ions.^[12] They seem similar to this Ti-based surface integrated layer and bulk doping, but there are three fundamental differences: 1) In order to make full use of doping in Li-sites to suppress the generation of surface lithium vacancy upon delithiation, doping of Lisites are controlled to occur only on the surface integrated layer; 2) Doping of Li-sites induces the formation of continuous and uniform spinel-like rocksalt structure Fd-3m phase on the particle surface; 3) In the bulk, Ti ions are partially occupied TM sites to mitigate surface structural evolution towards the bulk.

16163028, 2021, 14, Downloaded from https://advanced.onlinelibrary.wiley.com/doi/10.1002/adfm.202009310 by University Town Of Shenzhen, Wiley Online Library on [24/11/2025]. See the Terms and Conditions (https://onlinelibrary.wiley.com/terms

and-conditions) on Wiley Online Library for rules of use; OA articles are governed by the applicable Creative Commons

Figure 2. The STEM images of Ti-150 sample: a) low magnification, b) the corresponding selected area electron diffraction pattern, c-i) HAADF-STEM images of different regions.

These three differences may be very useful in suppressing the generation of surface Li vacancies during Li extraction, undesirable interfacial reactions, and structural evolution.

Figure 3 and Figure S6, Supporting Information, illustrate the electrochemical performance of PM and Ti-treated samples tested between 2.0 and 4.8 V. The initial discharge capacity of PM, Ti-150 and Ti-100 samples at 0.1 C is 283.3, 276.9 and 269.9 mAh g⁻¹, respectively, as displayed in Figure S6a-c, Supporting Information. All the initial charge/discharge curves of the three samples consist of a slope region and a long plateau. The slope region (3.9-4.36 V) is attributed to the extraction of lithium ions from the layered structure and the oxidation of Ni²⁺. [16] In addition, the long plateau above 4.5 V aligns with the Li-ion extraction process and oxygen release from the Li₂MnO₃ component which lead to a large initial irreversible capacity loss, as well as the formation of MnO₂-like phase.^[17] Compared with PM sample, Ti-treated samples seem to exhibit better stability towards the voltage decay regarding the evolution of their discharge profiles in 200 cycles, as exhibited in Figure 3a-c. This improved voltage stability is ascribed to the combination of surface Ti-based integrated layer and bulk Ti-doping which prevents the cathode against layered-to-spinel phase transition during cycling.

To investigate the influence of surface Ti-based integrated layer and bulk Ti-doping on phase transition, the corresponding

dO/dV curves of typical cycles for the three samples are plotted in Figure 3d-f and Figure S6d-f, Supporting Information. For all samples, the peak pair at about 4.0 V region is ascribed to extraction and insertion of Li+ from the Li layer along with Ni^{2+/4+} redox similar to a normal layered structure (R-3m space group).[18] The other peak couple at about 3.0 V corresponds to the redox of Mn4+/3+ in spinel phase and layered structure. [19] These peaks are also observed in cyclic voltammetry (CV) curves, as presented in Figure S7, Supporting Information. With further cycling, the oxidation peaks of PM sample (Figure 3d) move towards high potential, while the reduction peaks show a big shift to lower potential. This suggests significant cathode-electrolyte interfacial reactions have been occurring during cycling, which leads to an improved polarization. Differently, most of redox peaks for Ti-treated samples maintain stable position with cycling (Figure 3e,f). For the dQ/dV curve of the 200th cycle, the reduction peak position of Mn⁴⁺/Mn³⁺ for PM sample has entirely shifted to spinel region, while that for Ti-treated samples almost locates in its original position. These results of dQ/dV curves prove surface Ti-based integrated layer and bulk Ti-doping greatly helps to mitigate interfacial reaction and stabilize lattice structure.

The cycling performance of PM, Ti-100, and Ti-150 samples at 1 C is shown in Figure 3g. After 200 cycles, the discharge capacity of PM electrode decreases from 254.5 to 159.8 mAh $\rm g^{-1}$,

www.afm-journal.de

16163028, 2021, 14, Downloaded from https://advanced.onlinelibrary.wiley.com/doi/10.1002/adfm.202009310 by University Town Of Shenzhen, Wiley Online Library on [24/11/2025]. See the Terms

onditions) on Wiley Online Library for rules of use; OA articles are governed by the applicable Creative Commons License

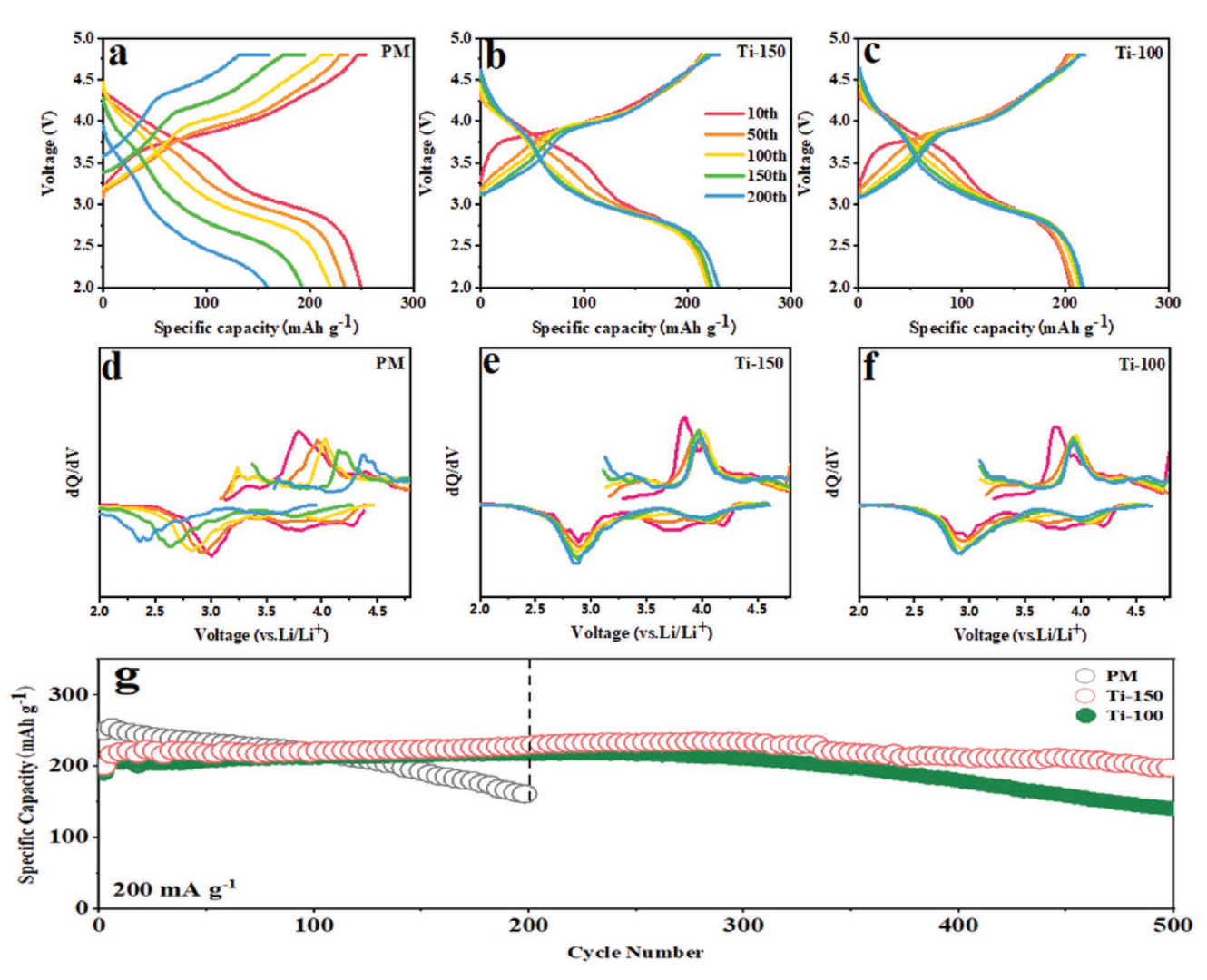


Figure 3. Electrochemical performances of all samples. a–c) The charge-discharge curves of PM, Ti-150, and Ti-100 cathode materials at 1 C between 2.0 and 4.8 V at room temperature, d–f) the corresponding dQ/dV curves of samples in the voltage range of 2.0–4.8 V for the 10th, 50th, 100th, 150th and 200th cycles, and g) extra-long cycling life at 1 C of the three samples.

exhibiting a serious capacity fading. The cycling stability of Ti-treated samples has a great improvement. The discharge capacity of Ti-150 sample is still as large as 235.0 mAh g⁻¹ after 300 cycles. Even after 500 cycles, its capacity retention ratio is still higher than 85%. SEM images (Figure 1g,f) indicate the fracture morphology and large cracks in Ti-150 sample, which are very slight in Ti-100 sample. However, the long cycling stability of Ti-150 sample is much better than that of Ti-100 sample, which is due to the following reasons. The fracture morphology and large cracks of Ti-150 sample are caused by the precursors with some fragile microspheres which are easy to break during the treated process. Without treatment, these fragile microspheres are likely to crack upon long cycling. Note that the newly generated cracks during cycling should lack surface Ti-based integrated layer. It is very unfavorable for the stability of the surface structure. Differently, surface Ti-based integrated layer can be built in the cracks generated during the treated process. That is, the treated process simply breaks the fragile microspheres ahead of time to protect its surface.

Therefore, the Ti-150 sample show better long cycling stability than the Ti-100 sample.

As presented in Figure S8, Supporting Information, the voltage decay rate from the 30th to 200th cycle of Ti-150 and Ti-100 is $\approx\!1.06$ and 1.05 mV/cycle, respectively, while that of PM sample is higher than 3.54 mV/cycle. The voltage decay rate from the 30th to the 500th cycle of Ti-150 and Ti-100 is as small as 0.72 and 0.90 mV/cycle, respectively. Notably, both the discharge capacity of Ti-100 and Ti-150 samples displays a very slow enhanced process. Their maximum discharge capacity is 219.3 mAh g⁻¹ at the 223rd cycle and 235.2 mAh g⁻¹ at the 278th cycle, respectively. Such a slow enhanced process is closely related to surface Ti-based integrated layer, which acts as a wall and greatly mitigates the activation rate of Li₂MnO₃ component. In addition, the inhibition of surface Ti-based integrated layer on interfacial reactions also ensures slow growth of discharge capacity.

To determine the surface oxidation state of Mn in PM, Ti-150, and Ti-100 samples, Mn 3s and Mn 2p spectra are analyzed in

16163028, 2021, 14, Downloaded from https://advanced.onlinelibrary.wiley.com/doi/10.1002/adfm.202009310 by University Town Of Shenzhen, Wiley Online Library on [24/11/2025]. See the Terms and Conditions

onditions) on Wiley Online Library for rules of use; OA articles are governed by the applicable Creative Commons License

combination. Before cycling, the binding energy of all Mn $2p_{3/2}$ peaks for as-prepared PM, Ti-150, and Ti-100 samples locates at >642 eV region, and they all have a full width at half-maximum (FWHM) much less than 3 eV (Figure S9, Supporting Information). It indicates that Mn ions in the three samples are present as Mn⁴⁺.[^{20]} This verdict is further demonstrated by Mn 3s spectra, as displayed in Figure S10a–c, Supporting Information. The splitting energy of the double peaks in Mn 3s spectra of PM, Ti-150, and Ti-100 samples are severally 4.55, 4.55, and 4.61 eV, conforming to Mn ions with a valence state of +4.[^{21]} In addition, Ni 2p spectra of as-prepared PM, Ti-150, and Ti-100 samples are also exhibited in Figure S11, Supporting Information. Their splitting values between Ni $2p_{1/2}$ and $2p_{3/2}$ peaks are 17.37, 17.42, and 17.45 eV, respectively. It suggests that the valence state of Ni ions in the three samples is +2.[^{22]}

After 100 cycles, the full width at half maximum (FWHM) of all Mn $2p_{3/2}$ peaks for cycled PM, Ti-150, and Ti-100 samples

is over +3 eV, and the splitting energy of the double peaks in their Mn 3s spectra is also larger than 4.7 eV, as presented in Figure S9d–f, Supporting Information, and Figure 4a–c. All of these prove that part Mn³+ ions emerge in the cycled samples. In addition, the splitting value for cycled PM, Ti-150 and Ti-100 samples is 5.47, 4.95, and 4.96 eV, and the ratio of Mn³+ to Mn⁴+ based on the fitted results of Mn 2p spectra is 0.86, 0.15, and 0.19, respectively. These data demonstrate that the introduction of surface Ti-based integrated layer effectively inhibit interfacial reactions, which is beneficial to the stability of redox couples and bulk structure during cycling.

The surface corrosion of PM, Ti-150, and Ti-100 samples before and after cycling is further investigated by using O 1s spectra (Figure 4d–f; Figure S10d–f, Supporting Information). Before cycling, there is a strong peak at 529.4 eV, corresponding to the lattice oxygen of LLOs, [23] which gradually shifts to higher binding energy (529.9 and 529.7 eV) for the Ti-treated samples.

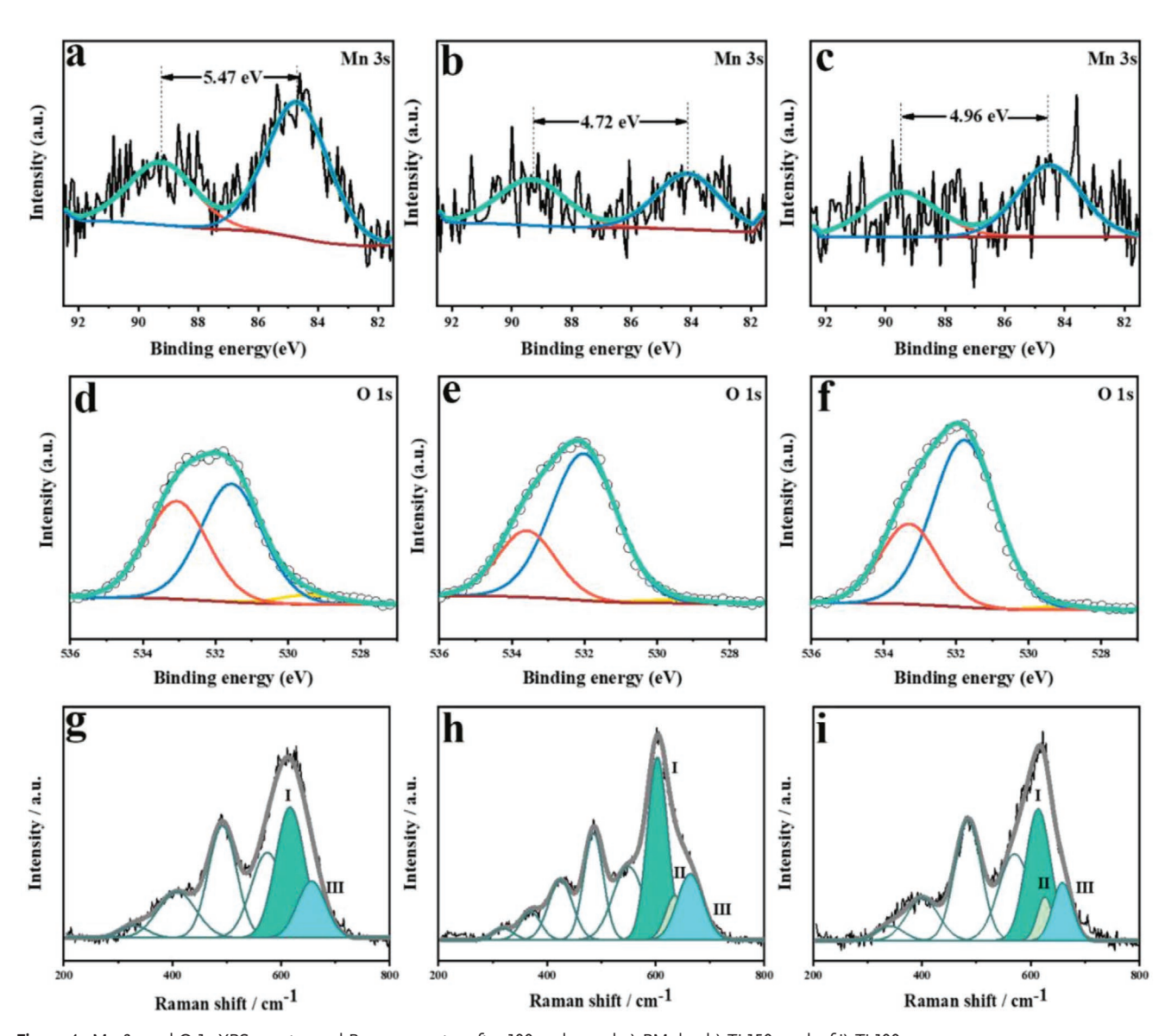


Figure 4. Mn 3s and O 1s XPS spectra and Raman spectra after 100 cycles. a,d,g) PM, b,e,h) Ti-150, and c,f,i) Ti-100.

16163028, 2021, 14, Downloaded from https://advanced

.com/doi/10.1002/adfm.202009310 by University Town Of Shenzhen, Wiley Online Library on [24/11/2025]. See the Terms and Conditions (https://original.com/doi/10.1002/adfm.202009310 by University Town Of Shenzhen, Wiley Online Library on [24/11/2025]. See the Terms and Conditions (https://original.com/doi/10.1002/adfm.202009310 by University Town Of Shenzhen, Wiley Online Library on [24/11/2025]. See the Terms and Conditions (https://original.com/doi/10.1002/adfm.202009310 by University Town Of Shenzhen, Wiley Online Library on [24/11/2025]. See the Terms and Conditions (https://original.com/doi/10.1002/adfm.202009310 by University Town Of Shenzhen, Wiley Online Library on [24/11/2025]. See the Terms and Conditions (https://original.com/doi/10.1002/adfm.202009310 by University Town Of Shenzhen, Wiley Online Library on [24/11/2025]. See the Terms and Conditions (https://original.com/doi/10.1002/adfm.202009310 by University Town Of Shenzhen, Wiley Online Library on [24/11/2025]. See the Terms and Condition (https://original.com/doi/10.1002/adfm.202009310 by University Town Of Shenzhen, Wiley Online Library on [24/11/2025]. See the Terms and Condition (https://original.com/doi/10.1002/adfm.202009310 by University Town Of Shenzhen, Wiley Online Library on [24/11/2025]. See the Terms and Condition (https://original.com/doi/10.1002/adfm.202009).

and-conditions) on Wiley Online Library for rules of use; OA articles are governed by the applicable Creative Commons

It is because the introduction of Ti atoms enhances electronic interaction. The peak I at 533.1 eV is assigned to active oxygen species on the surface or the impurity of adsorbed species, such as $\rm Li_2CO_3$, [^{24]} and the peak II at 531.6 eV corresponds to surface oxidized species. [^{25]} The relative intensity of both the peak I and II for PM sample is higher than that for Ti-150 and Ti-100 samples, which suggests PM sample has a sensitive surface which is rich in residual lithium.

It is hard to observe the peak of lattice oxygen in O 1s spectra of PM, Ti-150, and Ti-100 samples after 100 cycles, as shown in Figure 4d–f. The disappearance of this peak suggests all samples undergo interfacial reactions during cycling. Some by-products are deposited on the surface of active materials, which affects the detection of XPS on lattice oxygen due to the limitation of detection depth. Table S3, Supporting Information, exhibits the ratios of the peak I/II for the cycled samples, in which the value of cycled PM sample (0.83) is about twice as much as that of cycled Ti-treated samples (0.40 and 0.43). This indicates that cathode-electrolyte interfacial reactions for PM sample is more serious than that for Ti-treated samples.^[26] Therefore, O 1s data further demonstrate that the surface Ti-based integrated layer effectively mitigates interfacial reactions during cycling.

The Raman spectroscopy was employed to provide information on the general surface structure of a material, and investigate the surface phase evolution of cycled electrodes. Figure S10g-i, Supporting Information, and Figure 4g-i compare the Raman spectra of PM and Ti-treated samples before and after cycling. Being consistent with the results of XRD and STEM analysis, the signals of LiMO₂ and Li₂MnO₃ components are clearly observed in Raman spectra of all the three asprepared samples. The peak I at 605 cm⁻¹ is the feature of A_{1g} vibration mode for layered LiMO₂ structure, [27] and the other strong peak at 630 cm⁻¹ (peak II) can be assigned to the A_a mode of monoclinic Li₂MnO₃ structure.^[28] Differently, a slight peak at 655 cm⁻¹ (peak III) only emerges in the Raman spectra of Ti-treated samples, while is absent in that of PM sample, as presented in Figure S10g-i, Supporting Information. The peak III is attributed to the spinel-like phase. [29] This is because some Ti ions replace part of surface Li sites in Li layer and induce the formation of spinel-like phase. Therefore, the combination of STEM and Raman results demonstrate that the surface Tibased integrated layer is a spinel-like rocksalt structure with Fd-3m space group.

After 100 cycles, Raman spectra of cycled PM and Ti-treated samples are shown in Figure 4g–i. The peak II assigned to monoclinic Li₂MnO₃ structure is hard to be observed in the Raman spectrum of cycled PM sample, while has a few reservations in that of cycled Ti-treated samples. The typical diffraction peak of monoclinic Li₂MnO₃ structure still exists in XRD pattern of cycled Ti-treated samples and absents in that of cycled PM sample, as presented in Figure S12, Supporting Information. These phenomena suggest that Li₂MnO₃ component has been activated completely in cycled PM sample, and the activated process needs to continue in cycled Ti-treated samples even after 100 cycles. The very slow activated procedure is related to the continuous and uniform surface Ti-based integrated layer:

1) Strong Ti—O bonds moderately increase the resistance, as demonstrated by electrochemical impedance spectroscopy (EIS;

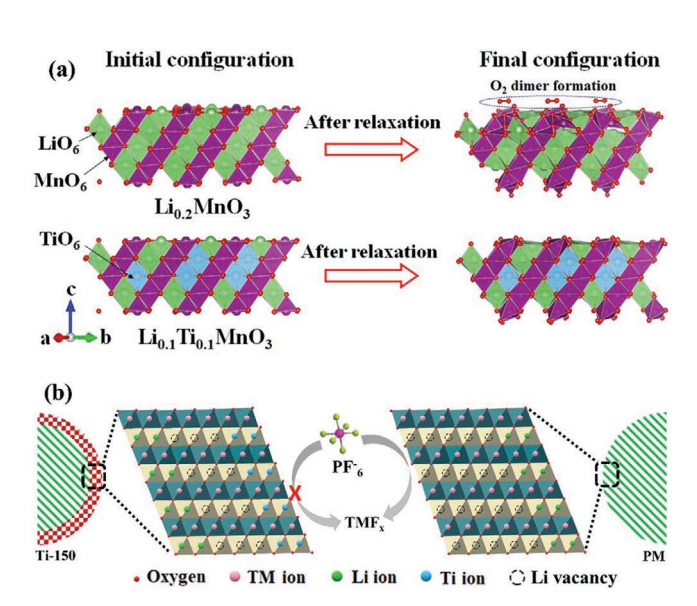


Figure 5. a) The effect of partial Ti in Li-sites on structural stability under charging state simulated by DFT calculations, and b) schematic illustration of the important function of surface Ti-based integrated layer at high work voltage.

Figure S13 and Table S4, Supporting Information); 2) Ti in Li sites hinder the transport of Li-ions, resulting in a low diffusion coefficient of Li⁺ (Figure S14 and Table S5, Supporting Information). In addition, the value of area ratio for the peak III in the Raman spectrum of cycled PM sample has increased by 29.65%, while that of cycled Ti-100 and Ti-150 samples has only increased by 11.53% and 15.10%, respectively, as listed in Table S6, Supporting Information. This indicates that the combination of surface Ti-based integrated layer and bulk Ti-doping significantly mitigates the layered-to-spinel evolution.

From the above discussion, we confirm that both bulk Tidoping and surface Ti-based integrated layer have a key role in the structural and interfacial stability of LLO cathodes under deep delithiation. Density functional theory (DFT) calculations were employed to interpret the effect of partial Ti in Lisites on structural stability under charging state, as displayed in Figure 5a. The slab surface was modeled using four layers monoclinic-Li₂MnO₃ (131) surface, which has been proven to be the most stable surface of layered metal oxides and is equivalent to the rock-salt (001) surface. To simulate the charged state of Li₂MnO₃, we deleted Li-ions from the Li₂MnO₃ (131) surface. The Ti-doped Li₂MnO₃ were also modeled by replacing partial Li-ions with Ti ions. The stability of slab surfaces was assessed by relaxing the configurations after the consideration of lithium extraction. The right insets suggest that two adjacent O-ions on Li_{0.2}MnO₃ (131) surface underwent dimerization and formed an oxygen dimer with an O-O bond length of 1.24 Å. However, the Ti-doped (131) surfaces maintain stable polyhedrons after relaxation. DFT calculations demonstrate partial Ti in Li-sites can greatly enhance the structural stability of LLO cathodes under deep charged state.

In addition, the important function of surface Ti-based integrated layer at high work voltage is debated vividly in terms of the schematic illustration in Figure 5b. When LLO cathodes situate in deep delithiation state, there are lots of Li vacancies in



____ MATERIALS
www.afm-iournal.de

ADVANCED FUNCTIONAL MATERIALS

crystal lattice. At this point, the Mn and Ni ions tend to migrate towards the Li vacancies to form a new structure with low energy. Most of the migration in bulk is inhibited very well by bulk doping, especially the cations that can form stronger M–O bonds, such as Ti, V, Cr, and Zr based on the density function theory (DFT) calculations of Wang et al. [7c] However, the surface migration phenomenon is extremely difficult to be controlled by single bulk doping due to multiple drives of cathode-electrolyte interfacial reactions, Li and oxygen vacancies. These are why phase evolution always begins on the surface of layered cathodes.

This work discovers that the voltage decay and capacity fading of LLO cathodes are effectively mitigated by the combination of surface Ti-based integrated layer and bulk Ti-doping. It is due to the following reasons: 1) Continuous and uniform surface Ti-based integrated layer not only prevents direct contact between electrolyte and active materials, but also suppresses the generation of Li vacancies in several atomic layers on surface. It therefore greatly inhibits interfacial reactions and surface structure evolution; and 2) electrochemical inert Ti⁴⁺ ions also play a pillar, which further restrains the migration of Mn and Ni ions and improves the structure stability. Note that we also found excessive Ti-treatment negatively impacts cycling performance (Figure S2, Supporting Information). The transport channel of Li ions is impeded when too many atomic layers of surface Li ions are fully replaced by Ti ions. Therefore, moderate Ti-treated amount (≈0.5% in this work) not only improves the voltage and capacity stability, but also allows Li ions' transport smoothly in the electrode.

3. Conclusions

In summary, STEM and EDX-mapping prove bulk Ti-doping and surface Ti-based integrated layer are constructed successfully by the molten-salt-assisted solvothermal-treatment method. Li ions on surface in several atom layers are completely replaced by Ti ions, forming a continuous and uniform surface Ti-based integrated layer. Electrochemical measurement indicates that the capacity retention of Ti-150 sample is still higher than 85% after 500 cycles, and its voltage decay rate from the 30th to the 500th cycle is as small as 0.72 mV/cycle. In terms of spectral results and DFT calculations, such excellent voltage and capacity stability is because bulk Ti-doping mitigate the migration of Mn and Ni ions in bulk due to the stronger Ti-O bonds, while surface Ti-based integrated layer significantly suppresses interfacial reactions and surface structure evolution by building a very continuous and uniform wall to prevent the generation of surface Li vacancies and direct contact between electrolyte and active materials. The construction of Ti-based integrated layer and its combination with bulk doping provide a new direction for the development of advanced Li-rich layered cathodes in the near future.

Supporting Information

Supporting Information is available from the Wiley Online Library or from the author.

Acknowledgements

The authors thank the funding supports of the National Natural Science Foundation of China (Project 51874104 and 52004070) and the Key Technology and Supporting Platform of Genetic Engineering of Materials under States Key Project of Research and Development Plan of China (Project 2016YFB0700600).

Conflict of Interest

The authors declare no conflict of interest.

Data Availability

Research data are not shared.

Keywords

capacity fading, interfacial reactions, Li-ion batteries, Li-rich layered cathodes, structure evolution, Ti-based integrated layer, voltage decay

Received: October 31, 2020 Revised: December 31, 2020 Published online: January 29, 2021 1616292. 2021, 14, Downloaded from https://advanced.onlinelibtrary.viely.com/doi/10.1002/adf.202009310 by University Town Of Shenzhen, Wiley Online Library on [24/11/2025]. See the Terms and Conditions (https://onlinelibrary.wiley.com/terms-and-conditions) on Wiley Online Library or rules of use; OA articles are governed by the applicable Creative Commons License

- [1] a) M. Li, J. Lu, Z. Chen, K. Amine, Adv. Mater. 2018, 30, 1800561;
 b) J. Wu, Y. Cao, H. Zhao, J. Mao, Z. Guo, Carbon Energy 2019, 1, 57;
 c) H. Liu, H. Guo, B. Liu, M. Liang, Z. Lv, K. R. Adair, X. Sun, Adv. Funct. Mater. 2018, 28, 1707480.
- [2] W. E. Gent, K. Lim, Y. Liang, Q. Li, T. Barnes, S. J. Ahn, K. H. Stone, M. McIntire, J. Hong, J. H. Song, Y. Li, A. Mehta, S. Ermon, T. Tyliszczak, D. Kilcoyne, D. Vine, J. H. Park, S. K. Doo, M. F. Toney, W. Yang, D. Prendergast, W. C. Chueh, *Nat. Commun.* 2017, 8, 2091.
- [3] a) A. Boulineau, L. Simonin, J. F. Colin, C. Bourbon, S. Patoux, Nano Lett. 2013, 13, 3857; b) D. Leanza, M. Mirolo, C. A. F. Vaz, P. Novák, M. E. Kazzi, Batteries Supercaps 2019, 2, 482.
- [4] S. Liu, Z. Liu, X. Shen, W. Li, Y. Gao, M. N. Banis, M. Li, K. Chen, L. Zhu, R. Yu, Z. Wang, X. Sun, G. Lu, Q. Kong, X. Bai, L. Chen, Adv. Energy Mater. 2018, 8, 1802105.
- [5] X. Zhang, I. Belharouak, L. Li, Y. Lei, J. W. Elam, A. Nie, X. Chen, R. S. Yassar, R. L. Axelbaum, Adv. Energy Mater. 2013, 3, 1299.
- [6] a) J. Ma, Y.-N. Zhou, Y. Gao, X. Yu, Q. Kong, L. Gu, Z. Wang, X.-Q. Yang, L. Chen, Chem. Mater. 2014, 26, 3256; b) P. Yan, J. Zheng, Z. K. Tang, A. Devaraj, G. Chen, K. Amine, J. G. Zhang, L. M. Liu, C. Wang, Nat. Nanotechnol. 2019, 14, 602.
- [7] a) C. Jacob, J. Jian, Q. Su, S. Verkhoturov, R. Guillemette, H. Wang, ACS Appl. Mater. Interfaces 2015, 7, 2433; b) E. Lee, K. A. Persson, Adv. Energy Mater. 2014, 4, 1400498; c) Y. Gao, X. Wang, J. Ma, Z. Wang, L. Chen, Chem. Mater. 2015, 27, 3456.
- [8] a) J. Zheng, P. Xu, M. Gu, J. Xiao, N. D. Browning, P. Yan, C. Wang, J.-G. Zhang, Chem. Mater. 2015, 27, 1381; b) L. Gu, D. D. Xiao, Y. S. Hu, H. Li, Y. Ikuhara, Adv. Mater. 2015, 27, 2134; c) J. M. Zheng, M. Gu, J. Xiao, P. J. Zuo, C. M. Wang, J. G. Zhang, Nano Lett. 2013, 13, 3824.
- [9] a) K. Ku, J. Hong, H. Kim, H. Park, W. M. Seong, S.-K. Jung, G. Yoon, K.-Y. Park, H. Kim, K. Kang, Adv. Energy Mater. 2018, 8, 1800606; b) S. Choi, A. Manthiram, J. Electrochem. Soc. 2002, 149, A1157





www.afm-journal.de

16163028, 2021, 14, Downloaded from https://advanced.onlinelibrary.wiley.com/doi/10.1002/adfm.202009310 by University Town Of Shenzhen, Wiley Online Library on [24/11/2025]. See the Terms

of use; OA articles are governed by the applicable Creative Commons

- [10] a) N. Yabuuchi, K. Yoshii, S. T. Myung, I. Nakai, S. Komaba, J. Am. Chem. Soc. 2011, 133, 4404; b) A. Boulineau, L. c. Simonin, J.-F. Colin, E. Canévet, L. Daniel, S. Patoux, Chem. Mater. 2012, 24, 3558
- [11] a) J.-N. Zhang, Q. Li, C. Ouyang, X. Yu, M. Ge, X. Huang, E. Hu, C. Ma, S. Li, R. Xiao, W. Yang, Y. Chu, Y. Liu, H. Yu, X.-Q. Yang, X. Huang, L. Chen, H. Li, Nat. Energy 2019, 4, 594; b) F. Wu, N. Liu, L. Chen, Y. Su, G. Tan, L. Bao, Q. Zhang, Y. Lu, J. Wang, S. Chen, J. Tan, Nano Energy 2019, 59, 50; c) H. P. Yang, H. H. Wu, M. Y. Ge, L. J. Li, Y. F. Yuan, Q. Yao, J. Chen, L. F. Xia, J. M. Zheng, Z. Y. Chen, J. Duan, K. Kisslinger, X. C. Zeng, W. K. Lee, Q. B. Zhang, J. Lu, Adv. Funct. Mater. 2019, 29, 13.
- [12] a) R. Yu, X. Wang, Y. Fu, L. Wang, S. Cai, M. Liu, B. Lu, G. Wang, D. Wang, Q. Ren, X. Yang, J. Mater. Chem. A 2016, 4, 4941; b) W. Yan, Y. Xie, J. Jiang, D. Sun, X. Ma, Z. Lan, Y. Jin, ACS Sustainable Chem. Eng. 2018, 6, 4625; c) X. Feng, Y. Gao, L. Ben, Z. Yang, Z. Wang, L. Chen, J. Power Sources 2016, 317, 74.
- [13] K. Luo, M. R. Roberts, N. Guerrini, N. Tapia-Ruiz, R. Hao, F. Massel, D. M. Pickup, S. Ramos, Y. S. Liu, J. Guo, A. V. Chadwick, L. C. Duda, P. G. Bruce, J. Am. Chem. Soc. 2016, 138, 11211.
- [14] a) J. Fan, G. Li, B. Li, D. Zhang, D. Chen, L. Li, ACS Appl. Mater. Interfaces 2019, 11, 19950; b) D. Luo, G. Li, C. Fu, J. Zheng, J. Fan, Q. Li, L. Li, Adv. Energy Mater. 2014, 4, 1400062.
- [15] B. Wu, X. Yang, X. Jiang, Y. Zhang, H. Shu, P. Gao, L. Liu, X. Wang, Adv. Funct. Mater. 2018, 28, 1803392.
- [16] E. M. Erickson, H. Sclar, F. Schipper, J. Liu, R. Tian, C. Ghanty, L. Burstein, N. Leifer, J. Grinblat, M. Talianker, J.-Y. Shin, J. K. Lampert, B. Markovsky, A. I. Frenkel, D. Aurbach, Adv. Energy Mater. 2017, 7, 1700708.
- [17] D. Luo, S. Fang, Q. Tian, L. Qu, L. Yang, S.-i. Hirano, *Nano Energy* 2016, 21, 198.

- [18] T. Lin, T. U. Schulli, Y. Hu, X. Zhu, Q. Gu, B. Luo, B. Cowie, L. Wang, Adv. Funct. Mater. 2020, 30, 1909192.
- [19] X. Ding, D. Luo, J. Cui, H. Xie, Q. Ren, Z. Lin, Angew. Chem., Int. Ed. 2020, 59, 7778.
- [20] S. Ivanova, E. Zhecheva, R. Stoyanova, D. Nihtianova, S. Wegner, P. Tzvetkova, S. Simova, J. Phys. Chem. C 2011, 115, 25170.
- [21] S. Shi, S. Zhang, Z. Wu, T. Wang, J. Zong, M. Zhao, G. Yang, J. Power Sources 2017, 337, 82.
- [22] J. C. Arrebola, A. Caballero, M. Cruz, L. Hernán, J. Morales, E. R. Castellón, Adv. Funct. Mater. 2006, 16, 1904.
- [23] S. Verdier, L. E. Ouatani, R. Dedryvere, F. Bonhomme, P. Biensan, D. Gonbeau, J. Electrochem. Soc. 2007, 154, A1088.
- [24] a) Z. Yang, G. Du, Q. Meng, Z. Guo, X. Yu, Z. Chen, T. Guo, R. Zeng, RSC. Adv. 2011, 1, 1834; b) Y. Zhao, M. Xia, X. Hu, Z. Zhao, Y. Wang, Z. Lv, Electrochim. Acta 2015, 174, 1167; c) Z. Sun, X. Wang, H. Zhao, S. W. Koh, J. Ge, Y. Zhao, P. Gao, G. Wang, H. Li, Carbon Energy 2020, 2, 122.
- [25] H. Z. Zhang, Q. Q. Qiao, G. R. Li, X. P. Gao, J. Mater. Chem. A 2014, 2, 7454.
- [26] a) E. Björklund, M. Göttlinger, K. Edström, R. Younesi, D. Brandell, Batteries Supercaps 2019, 3, 201; b) G. Zhao, Y. Zhang, Z. Gao, H. Li, S. Liu, S. Cai, X. Yang, H. Guo, X. Sun, ACS Energy Lett. 2020, 5, 1022.
- [27] J.-X. Huang, B. Li, B. Liu, B.-J. Liu, J.-B. Zhao, B. Ren, J. Power Sources 2016. 310. 85.
- [28] R. E. Ruther, A. F. Callender, H. Zhou, S. K. Martha, J. Nanda, J. Electrochem. Soc. 2014, 162, A98.
- [29] a) D. Liu, X. Fan, Z. Li, T. Liu, M. Sun, C. Qian, M. Ling, Y. Liu, C. Liang, Nano Energy 2019, 58, 786; b) D. Luo, X. Ding, J. Fan, Z. Zhang, P. Liu, X. Yang, J. Guo, S. Sun, Z. Lin, Angew. Chem., Int. Ed. 2020, 59, 23061.